A Low-Noise Transmission-Type Yttrium Iron Garnet Tuned Oscillator Based on a SiGe MMIC and Bond-Coupling Operating up to 48 GHz

Marcel van Delden, *Student Member, IEEE*, Nils Pohl, *Senior Member, IEEE*, Klaus Aufinger, *Member, IEEE*, Christoph Baer, *Member, IEEE*, and Thomas Musch, *Member, IEEE*

***Abstract*— Wideband and low-noise tunable oscillators at microwave frequencies are crucial within microwave frequency synthesizers and key to high-end measurement systems based on electromagnetic sensing in the microwave range as well as in the terahertz (THz) and sub-THz range. This paper presents a novel, wideband, and low-noise differential yttrium iron garnet (YIG) tuned oscillator. It is based on a SiGe monolithic microwave integrated circuit and a transmission-type YIG resonator. The integrated circuit contains a fully differential amplifier as a part of the oscillator core. The resonator was realized by two orthogonal, crossed pad-to-pad bonds and an YIG sphere, which is positioned between those bonds and the integrated circuit. To design and optimize the oscillator, an equivalent circuit modeling the resonator was developed. Concerning the tuning range and the phase noise, the results of the circuit simulations are in good agreement with the measurements. Two oscillators with different lengths of the inductive load transmission line were realized. First, the oscillator with a short transmission line offers very high-oscillation frequencies with a tuning range from 32.0 to 48.2 GHz. It exhibits an excellent phase noise of less than −119 dBc/Hz at an offset frequency of 100 kHz for oscillation frequencies up to 42 GHz. Second, the oscillator with a longer transmission line length offers a tuning range from 19.1 to 41.4 GHz. This configuration exhibits an excellent phase noise of less than −120 dBc/Hz at an offset frequency of 100 kHz for oscillation frequencies up to 38 GHz.**

***Index Terms*— Low noise source devices, microwave and millimeter wave oscillators, SiGe HBT circuits, ultra-wideband sources devices, yttrium iron garnet (YIG).**

I. Introduction

MICROWAVE frequency synthesizers are key to high-end measurement systems based on electromagnetic (EM) sensing in the microwave wave range as well as in the terahertz (THz) and sub-THz range. While they are generating directly the measurement signal in the microwave range [1], they act as the reference signal in THz and sub-THz measurement systems [2], [3]. In both cases, the performance of the measurement system in terms of resolution, precision, and accuracy is mostly determined by the bandwidth and phase noise of the synthesizer [1], [4], [5]. Improving this performance is not only beneficial for well-known applications, such as device characterization [6]–[8] as well as distance and velocity measurements [1], [9], [10], but it also enables various new fields of application. These new fields are, e.g., material characterization [11], [12], biomedical sensing [13], [14], security [2], [12], and plasma diagnostics [15].

Generally, high-end microwave frequency synthesizers utilize a wideband tunable oscillator, which generates the output signal. This oscillator is stabilized by the synthesizer, commonly by means of a phase-locked loop (PLL). While the PLL determines the close-in phase noise and controls the output frequency, the tunable oscillator defines the bandwidth. Moreover, the lower the phase noise of the tunable oscillator, the lower the loop bandwidth of the PLL and, thus, the integrated phase noise can be [16]. Three different state-of-the-art types of tunable oscillators are used in microwave frequency synthesizers.

First, voltage-controlled oscillators (VCOs) based on an *LC* tank resonator utilize a varactor to tune the output frequency. On the one hand, the entire VCO can be implemented in a single monolithic microwave integrated circuit (MMIC) [17], [18], which allows for low cost, weight, and size. On the other hand, the continuously tunable relative bandwidth is limited and the phase noise is only moderate [17], [18].

Second, tunable opto-electronic oscillators (TOEO) use sophisticated optical resonators to tune the output frequency in the microwave range. They offer a high bandwidth of up to more than one octave and low phase noise at the same time [19], [20]. However, TOEOs require at least a laser, an optical resonator, an electrooptic phase or amplitude modulator, a fast photodiode, a delay line as well as a filter, and an amplifier for microwave frequencies. High-performance TOEOs like [19], [20] require even more and sophisticated components. Thus, TOEOs are expensive and complex.

Manuscript received March 21, 2019; revised May 9, 2019; accepted May 29, 2019. This work was supported by the German Research Foundation (DFG) within the framework of the Collaborative Research Center TRR 196 "Mobile Material Characterization by Electromagnetic Sensing." This paper is an expanded version from the Radio and Wireless Symposium, Orlando, FL, USA, January 20–23, 2019. *(Corresponding author: Marcel van Delden.)*

M. van Delden, C. Baer, and T. Musch are with the Institute of Electronic Circuits, Ruhr University Bochum, 44801 Bochum, Germany (e-mail: marcel.vandelden@rub.de).

N. Pohl is with the Institute of Integrated Systems, Ruhr University Bochum, 44801 Bochum, Germany.

K. Aufinger is with Infineon Technologies AG, 85579 Neubiberg, Germany.

Color versions of one or more of the figures in this paper are available online at http://ieeexplore.ieee.org.

Digital Object Identifier 10.1109/TMTT.2019.2926293

Third, yttrium iron garnet (YIG) tunable oscillators (YTOs) utilize an YIG sphere as the resonator, whose resonance frequency is tuned by a magnetic field [21]. They offer a high bandwidth of up to more than one octave and low phase noise at the same time, like TOEOs. However, unlike TOEOs, YTOs do not exhibit critical spurs at high offset frequencies and exhibit a crucial lower noise floor [19], [20], [22], [23]. Moreover, YTOs have a crucial lower complexity. These advantages make YIG tuned oscillators favorable for high-end microwave frequency synthesizers. Typically, the adjustable magnetic field to tune the YTO is generated by the combination of a main coil and an FM coil [24]. The main coil is realized as a major electromagnet with ferromagnetic core and is used for slow, coarse tuning, as it generates the main part of the magnetic field. The FM coil is typically a small air coil and is used for fast, fine tuning. The FM coil allows to embed the YTO in a PLL for absolute and long-term frequency stability [25]. Moreover, the PLL can potentially compensate for temperature deviations and, in combination with a shielded housing, for disturbances generated by undesired external magnetic fields [26]. Although the state-of-the-art YTOs are not as complex as TOEOs, they commonly use sophisticated designs with discrete transistors on an alumina substrate, where the YIG sphere is coupled via transmission lines [22], [27]. Doing so, the generation of higher frequencies is challenging and the costs as well as the complexity are higher compared to an MMIC-based approach. Furthermore, an MMIC-based design allows for a differential circuitry, which is hardly feasible with a discrete design. Yet, only [28] presented an approach for a differential YTO using an MMIC.

In [23], we basically presented a novel, MMIC-based YTO concept and demonstrated a first approach with limited bandwidth. In Sections II and III, we expand the theoretical background of the concept and the modeling of the YIG, respectively. In Section IV, we describe the circuit design including simulations of the entire YTO utilizing the model from Section III. In Section V, we show the realization of the new YTO with more than an octave bandwidth as well as the measurement setup. In Section VI, we present and discuss the corresponding measurement results and compare them to those obtained in [23]. Moreover, we include a comparison with the state-of-the-art YTOs, VCOs, and TOEOs in Section VII.

II. Concept

The oscillation of a YTO is based on the electron spin precession of YIG, which exhibits a small ferromagnetic resonance linewidth and, thus, a high unloaded quality factor at frequencies between approximately 2 and 55 GHz [29]. The corresponding resonance frequency is

$$f_{\mathrm{res}} = \frac{\omega_{\mathrm{res}}}{2\pi} = \gamma \cdot (\mu \cdot H_0 + [N_{\mathrm{t}} - N_{\mathrm{z}}] \cdot M_0) \tag{1}$$

with the external dc magnetic field H_0, the gyromagnetic ratio of YIG $\gamma = 28$ GHz T^{-1}, the permeability μ of the environment, the magnetization saturation of YIG $M_0 = 0.178$ T, as well as the transversal and axial demagnetization factors N_{t} and N_{z}, respectively. As we use a sphere geometry, the demagnetization factors are $N_{\mathrm{t}} = N_{\mathrm{z}} = 1/3$. Therefore, the resonance frequency is only proportional to the external dc magnetic field

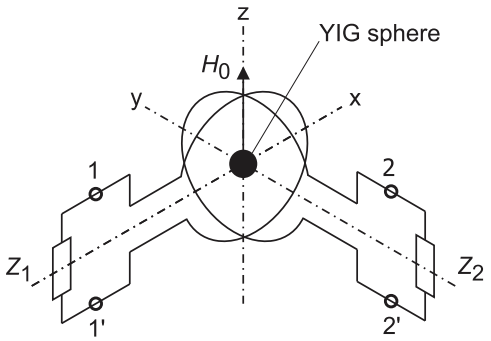

Fig. 1. Principle arrangement of the transmission-type YIG resonator with a YIG sphere in the center as well as two orthogonal coupling loops and the external magnetic field H_0, which is orthogonal to both coupling loops.

$$f_{\mathrm{res}} = \frac{\omega_{\mathrm{res}}}{2\pi} = \gamma \cdot \mu \cdot H_0. \tag{2}$$

To make use of this relationship, we arrange a YIG sphere as transmission-type resonator, as principally shown in Fig. 1. While the dc magnetic field H_0 is applied in the z-direction, two coupling loops 1 and 2 are in the xz and yz planes, respectively. Since the coupling loops are orthogonal to each other, usually no energy will be transferred between the corresponding port 1 and port 2. However, at the resonance frequency f_{res}, the precession of the electron spin causes a rotation of the ac magnetic field. Thus, only at this resonance frequency, energy will be transferred from port 1 to port 2 and vice versa with a phase shift of $-\pi/2$ and $\pi/2$, respectively [30]. The transmission-type resonator is favorable compared to a reflection-type resonator, because the first prohibits walker modes to be transmitted [31], which disturb the desired oscillation caused by the electron spin precession.

The two main components of the presented YTO are the MMIC and the YIG sphere. On the one hand, the MMIC enables the integration of several high-speed transistors. Thus, it includes a fully differential transmission amplifier as a part of the oscillator core and an output buffer to increase the output power and reduce the feedback of the external load to the oscillator core. On the other hand, the MMIC acts as a platform to directly couple the YIG sphere by means of two pairs of dedicated pads. These pads are connected by two crossed pad-to-pad bond wires. The YIG sphere is positioned directly between these orthogonal bond wires and the MMIC, as shown in Fig. 2. Thus, the combination of the bond wires and the YIG sphere create the aforementioned transmission-type YIG resonator. The pad pairs are acting as port 1 and port 2. This means that they are the differential input and output ports of the resonator as well as the output and input ports of the amplifier, respectively. The complete YTO is fully differential.

III. YIG Modeling

In order to conduct circuit simulations of the entire YTO and to optimize the design process, an appropriate model of

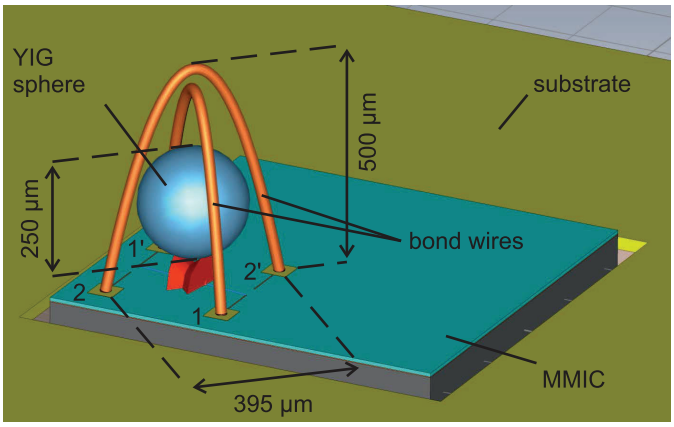

Fig. 2. Model used in the 3-D EM simulation to obtain parameters for the equivalent circuit of the YIG.

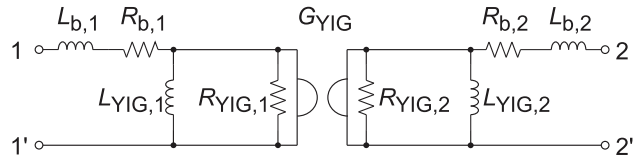

Fig. 3. Equivalent circuit of the transmission-type YIG resonator, used as model in the circuit simulation.

the YIG transmission resonator is required. Thus, we have developed an equivalent circuit to model the electrical behavior of the resonator between port 1 and port 2, as depicted in Fig. 3. First, the resistance and inductance of the coupling loops, that are the bond wires, are taken into account by means of $R_{b,1/2}$ and $L_{b,1/2}$. Second, the YIG sphere's resonance and coupling to the loops is modeled by the inductance $L_{YIG,1/2}$ and the gyrator with gyration resistance G_{YIG} [30]. These can be calculated according to

$$G_{YIG} = \mu \cdot V \cdot K_1 \cdot K_2 \cdot \omega_m \tag{3}$$

$$L_{YIG,1/2} = \mu \cdot V \cdot K_{1/2}^2 \cdot \omega_m/\omega_{res} \tag{4}$$

$$\omega_m = 2\pi \cdot \gamma \cdot M_0 \tag{5}$$

with the volume of the YIG sphere V. $K_{1/2}$ is the ratio of the ac magnetic field strength generated at the center of the YIG sphere to the current injected into port 1 and port 2, respectively. Third, the quality factor is modeled in the equivalent circuit by means of the resistance

$$R_{YIG,1/2} = 2 \cdot \omega_{res} \cdot L_{YIG,1/2} \cdot Q_{YIG}. \tag{6}$$

The unloaded quality factor Q_{YIG} of the YIG resonance can be calculated according [21]

$$Q_{YIG} = (\omega_{res} - \omega_m)/(2\pi \cdot \gamma \cdot \mu \Delta H) \tag{7}$$

with the ferromagnetic resonance linewidth of the YIG sphere ΔH, which depends on the quality and surface roughness of the YIG crystal. In order to achieve high performance, we utilized a high-quality YIG sphere with a ferromagnetic resonance linewidth of $\Delta H \leq 0.4\text{Oe} \approx 31.83$ A m^{-1} and a diameter of $d = 250$ µm, corresponding to a volume of $V = 0.008\ 18$ mm^3.

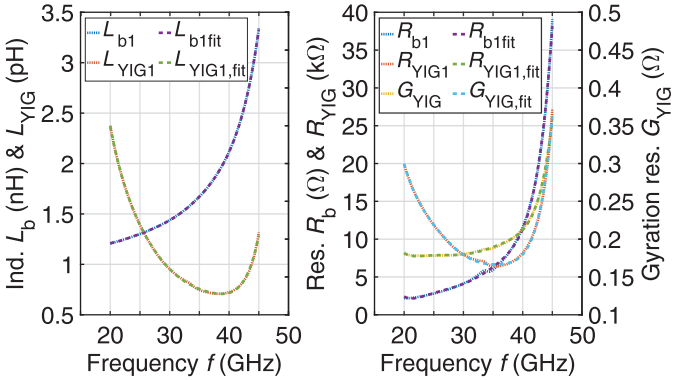

Fig. 4. Calculated frequency depending component values of the YIG resonator's equivalent circuit and the corresponding polynomial fits.

The magnetization saturation M_0 is the only direct parameter of the YIG sphere, which exhibit a considerable variation over temperature T. At room temperature, it is $M_0(300\text{ K}) = 0.178$ T and exhibits a temperature coefficient of approximately -0.33 mT K^{-1} [32]. As the utilized YIG sphere is highly polished with 0.05 µm, the ferromagnetic resonance linewidth ΔH [33] and the gyromagnetic ratio γ [32] are negligibly varying over the temperature range of interest. Furthermore, the thermal expansion coefficient of YIG is only 1.04×10^{-4}.

To obtain the component values of the equivalent circuit, we applied a 3-D EM simulation using CST MICROWAVE STUDIO. The corresponding model for the EM simulation is shown in Fig. 2, including the crucial dimensions. It contains the gold bond wires, the MMIC as well as the substrate with top and bottom copper ground planes to embed the MMIC. The YIG sphere is only visualized for illustration, and thus, it is only vacuum as the background material in the EM simulation. The MMIC model in the EM simulation consists of the silicon substrate and the front end of line including the dielectric, the copper ground planes, the copper transmission lines as well as the aluminum pads.

While the EM simulation directly provides $R_{b,1/2}$, $L_{b,1/2}$, and $K_{1/2}$, we calculated the other component values using equations (3)–(7). The resulting values of the components of the equivalent circuit are depicted in Fig. 4. As the resistances and inductances are comparable, that means $R_{b,1} \approx R_{b,2}$, $L_{b,1} \approx L_{b,2}$, $R_{YIG,1} \approx R_{YIG,2}$, and $L_{YIG,1} \approx L_{YIG,2}$, only the values with index 1 corresponding to port 1 are shown. In order to describe the nonconstant component values in the circuit simulator, we have fitted those by frequency-dependent sixth-order polynomials. These are in good agreement with the original values as shown in Fig. 4. Subsequently, we conducted circuit simulations of the equivalent circuit utilizing the polynomial fits. Fig. 5 shows the resulting transfer functions for exemplary resonance frequencies f_{res}. They exhibit a very small resonance linewidth of 6 MHz $\leq \Delta f_{res,3dB} \leq$ 16 MHz over the entire range of resonance frequencies. The attenuation at the resonance frequency is increasing with the resonance frequency from 5.8 dB at $f_{res} \approx 20$ GHz to 22 dB at $f_{res} \approx 44$ GHz. This occurs, as the resonance frequency of the YIG transmission resonator is getting closer to the self-resonance

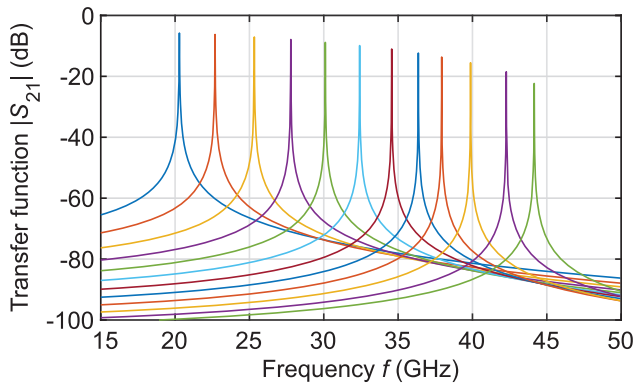

Fig. 5. Simulated transfer function $|S_{21}|$ of the YIG resonator's equivalent circuit for different resonance frequencies.

of the bond wires. The self-resonance can be observed by the highly increasing inductance $L_{\mathrm{b},1}$ and resistance $R_{\mathrm{b},1}$ of the bond wire toward higher frequencies, depicted in Fig. 4. From the EM simulations, the self-resonance can be estimated to be at approximately 51 GHz.

IV. Circuit Design

A. Technology

We designed the MMIC in Infineon's high-speed B11HFC 130-nm SiGe:C BiCMOS technology featuring heterojunction bipolar transistors with $f_t/f_{\max} = 250/370$ GHz [34]. Moreover, it offers MIM capacitors suitable for microwave frequencies, TaN resistors, a metal stack with six copper layers and a top aluminum layer as well as aluminum pads. The use of bipolar transistors is crucial for low phase noise of the oscillator, as they exhibit a low flicker noise corner compared to MOS transistors. This is due to the fact that the active region of bipolar transistors is vertical within the bulk silicon, whereas the active region of MOS transistors is horizontal along the surface of the silicon [35].

B. Circuitry

The schematic of the oscillator is depicted in Fig. 6. The oscillator core consists of a fully differential common base amplifier. The pads 1 and 1', corresponding to port 1 from Fig. 1 and Fig. 3, are connected to the collectors of the transistors $\mathrm{T}_1/\mathrm{T}_1'$. Thus, the differential output signal of the amplifier is coupled to the YIG sphere via the bond wire between those pads. As described in Section II, the YIG sphere transfers the signal at the resonance frequency to the second bond wire between the pads 2 and 2', corresponding to port 2 from Figs. 1 and 3. These pads are connected to the emitters of the transistors $\mathrm{T}_1/\mathrm{T}_1'$. In order to amplify the differential mode signal and reject the common mode signal, the emitters are decoupled/connected by the inductance L_0/L_0'. Subsequently, the differential signal is amplified from the emitters to the collectors with the inductive loads $L_{\mathrm{L}}/L_{\mathrm{L}}'$.

On the one hand, inductive loads exhibit low noise, which is favorable in oscillators. On the other hand, the inductive loads influence the bandwidth of the YTO, as the impedance of the

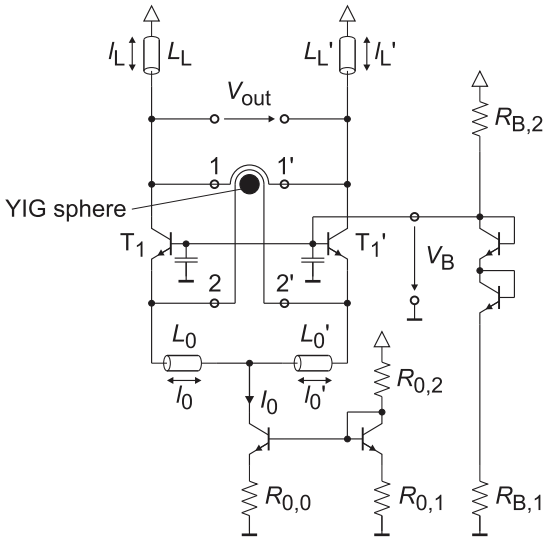

Fig. 6. Schematic of the fully differential oscillator core with YIG sphere including the biasing.

inductive load and, thus, the gain of the amplifier decreases toward lower frequencies. However, this behavior is desired, as it partially compensates the decreasing attenuation factor of the YIG resonator toward lower resonance frequencies, as described in Section III. As a result, the variation in the loop gain in the range of the oscillation frequencies is reduced. As the transistors $\mathrm{T}_1/\mathrm{T}_1'$ are operating in large signal mode, this also reduces the variation in the operating conditions of the transistors. Thus, the transistor design can be optimized for a wide range of oscillation frequencies. Moreover, the value of the inductive load influences the self-resonance caused by the parallel arrangement of the load inductance $L_{\mathrm{L}}/L_{\mathrm{L}}'$ and the bond wire at port 1. Thus, in principle, the range of oscillation frequencies can be shifted to higher or lower frequencies by decreasing or increasing the load inductance. This is still feasible after fabrication, as the inductances $L_{\mathrm{L}}/L_{\mathrm{L}}'$ as well as L_0/L_0' are realized as transmission lines with the lengths $l_{\mathrm{L}}/l_{\mathrm{L}}'$ and l_0/l_0', respectively. Thus, the length and, therefore, the inductance of the transmission lines can be adjusted by means of fuses. In this work, the length $l_0 = l_0' \approx 950$ μm is constant, while the length $l_{\mathrm{L}}/l_{\mathrm{L}}'$ is 180 μm and 260 μm, respectively, as described in the following.

The emitter bias current $I_0 = 25$ mA as well as the base bias voltage $V_{\mathrm{B}} = 1.6$ V are applied at the symmetry point between the transistors $\mathrm{T}_1/\mathrm{T}_1'$ and the supply voltage is 3 V. The appropriate biasing is realized by the resistors in Fig. 6, which are chosen to $R_{0,0} = 12\ \Omega$, $R_{0,1} = 60\ \Omega$, $R_{0,2} = 360\ \Omega$, $R_{\mathrm{B},1} = 50\ \Omega$, and $R_{\mathrm{B},2} = 290\ \Omega$. To maintain a high gain of the common base amplifier, the capacitors at each base of the transistors $\mathrm{T}_1/\mathrm{T}_1'$ are designed with 400 fF. Furthermore, an output buffer is connected to V_{out} at the collectors of the transistors $\mathrm{T}_1/\mathrm{T}_1'$. This buffer increases the output power and reduces the feedback from external load to the oscillator core, which can disturb the oscillation and cause undesired modulations as well as spurious. The buffer is realized as a common differential amplifier and is ac coupled at the input as well as the output.

C. Simulations

To simulate the entire YTO with the Cadence Specter circuit simulator, we applied the equivalent circuit from Section III, which is connected to port 1 and port 2. First, we have simulated the oscillator with a short transmission line $l_\mathrm{L} = l'_\mathrm{L} = 180\ \mu$m. This results in a tuning range of 30.9 GHz $\leq f_\mathrm{osc} \leq$ 49.3 GHz, while maintaining an output power of -3 dBm $\leq P_\mathrm{out} \leq$ 1 dBm, as depicted in Fig. 7 (top). At the same time, the phase noise at an offset frequency of $\Delta f = 100$ kHz is $L_{\Delta f=100\ \mathrm{kHz}} < -117$ dBc/Hz for oscillation frequencies $f_\mathrm{osc} \leq 42$ GHz and -125 dBc/Hz $\leq L_{\Delta f=100\ \mathrm{kHz}} \leq -98$dBc/Hz in the entire tuning range. Second, we simulated the YTO with a longer transmission line length $l_\mathrm{L} = l'_\mathrm{L} = 260\ \mu$m. Whereas, this attests an ultrawide tuning range of 16.3 GHz $\leq f_\mathrm{osc} \leq$ 45.3 GHz, while maintaining an output power of -6.3 dBm $\leq P_\mathrm{out} \leq -1.7$ dBm, as depicted in Fig. 7 (bottom). This adjustment exhibits a low phase noise of $L_{\Delta f=100\ \mathrm{kHz}} < -117$dBc/Hz for frequencies 16.3 GHz $\leq f_\mathrm{osc} \leq 40$ GHz and -127dBc/Hz $\leq L_{\Delta f=100\ \mathrm{kHz}} \leq -102$dBc/Hz in the entire tuning range. The phase noise increases toward higher oscillation frequencies, as the frequencies are getting close to the self-resonance of the bond wires.

D. Influence of Temperature and Orthogonality

To investigate the behavior of the YTO itself over the temperature, we applied the temperature dependencies from Section III to the YIG model and used the thermal modeling of the MMIC components from the process design kit. In the temperature range from 0 °C $\leq T \leq$ 80 °C, the resonance frequency, the phase noise, and the output power are only varying by 372 MHz, 2 dB, and 1 dB, respectively. However, the corresponding maximum frequency deviation of 103ppm/K can be compensated, if the YTO is embedded in a PLL.

The considerations, the YIG modeling, and the circuit simulations above are referring to orthogonal coupling loops. However, in practice, there are parts of the coupling loops, which are not perfectly orthogonal. On the one hand, the wedges of the bonds are not perfectly in the center of the pads, which results in a slight deviation of the angle between the loops. On the other hand, the bond wires are not straight lines in one plane and exhibit slight bends and buckles, which causes several not orthogonal sections. These deviations from perfect orthogonality have two major effects on the YTO.

First, the deviation from the orthogonality of the angle between the coupling loops $\Delta\varphi$ is directly added to the phase of the transfer function of the resonator φ_r. The phase of the transfer function close to the resonance frequency is approximately

$$\varphi_\mathrm{r} = \arg(S_{21}) = -\arctan\left(2 \cdot Q_\mathrm{L} \frac{\Delta\omega}{\omega res}\right) - \frac{\pi}{2} + \Delta\varphi \quad (8)$$

with the loaded quality factor of the YIG resonator Q_L and the offset from the angular resonance frequency $\Delta\omega$. Equation (8) is based on the well-known generic phase of the transfer function of transmission resonators and takes the aforementioned phase shift of $-\pi/2$ in the forward direction

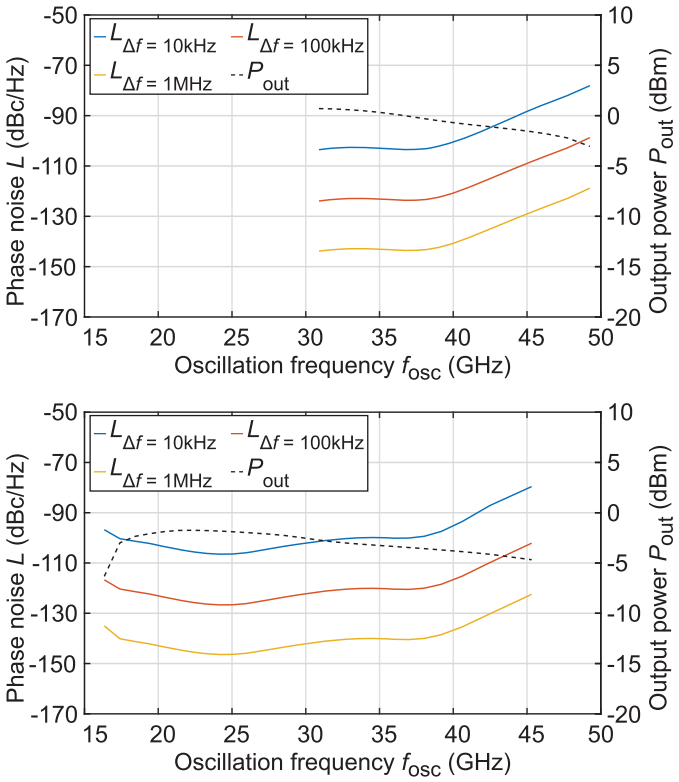

Fig. 7. Simulated phase noise L at different offset frequencies Δf and output power P_out as a function of the oscillation frequency f_osc for the YTO with a length of the load transmission line of $l_\mathrm{L} = l'_\mathrm{L} = 180\ \mu$m (top) and $l_\mathrm{L} = l'_\mathrm{L} = 260\ \mu$m (bottom).

into account, which is caused by the YIG and modeled by the gyrator. The self-resonance of the bond wires is neglected, as it is far enough from the resonance frequency. Applying (8) and presuming a loaded quality factor of about $Q_\mathrm{L} = 1500$, the shift of the frequency and the decrease of the quality factor is only less than 27.7 MHz and 101, respectively, for angle deviations $|\Delta\varphi| \leq 15°$ over the entire range of 16.3 GHz $\leq f_\mathrm{res} \leq$ 49.3 GHz.

Second, the deviation from orthogonality of the angle between the coupling loops causes an inductive coupling of the loops. Thus, an ac signal will be transferred between the ports 1 and 2 even without the YIG. To investigate the effect of this direct inductive coupling, we applied EM simulations like in Section III, but the bond wires were modeled with multiple deviation angles in the range of $-30° \leq \Delta\varphi \leq 30°$. In contrast to the circuit simulations above, the scattering parameters from the EM simulations are directly utilized as connecting element between port 1 and port 2 instead of the YIG model. Based on this, again circuit simulations were applied to investigate the stability of the circuit. As a result, this circuit does not exhibit any actual oscillations in the simulations for deviation angles $-30° \leq \Delta\varphi \leq 30°$. Thus, even with not perfect orthogonal coupling loops, there will be no oscillation except from the YIG.

V. Realization and Measurement Setup

Fig. 8 (top) shows a photograph of the realized MMIC. It occupies an area of approximately 400 μm^2, including the

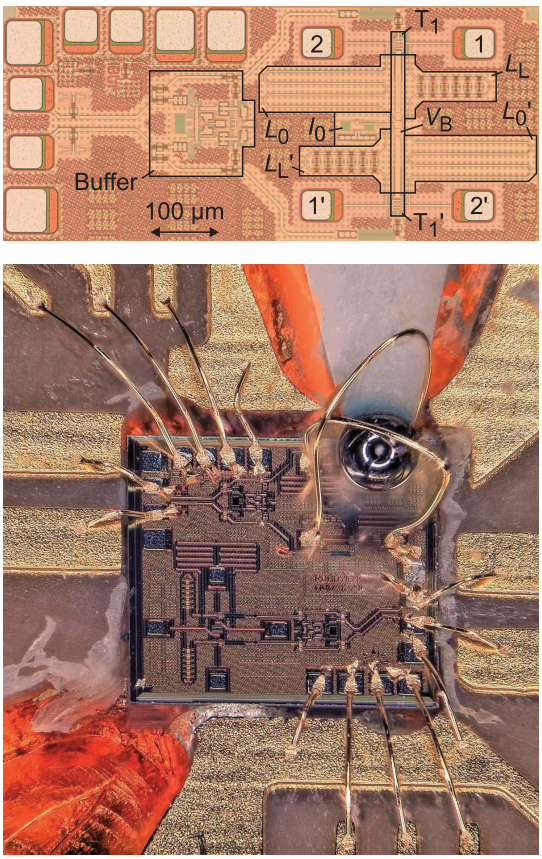

Fig. 8. Detailed photograph of the MMIC (top) as well photograph of the realized oscillator with YIG sphere, MMIC, coupling bonds, and transmission line (bottom).

pads for the microwave output signal as well as the supply. The area of the core, which is the rectangle defined by the pads 1, 1', 2, and 2', is 340 μm^2. The fuses to adjust the length of the transmission line are visible within the frame of $L_\mathrm{L}/L_\mathrm{L}'$. In order to create the YTO, the MMIC was embedded in a Rogers RT/duroid 5880 substrate with a gold-plated 9 μm top copper layer and a 1 mm bottom copper layer, as shown in Fig. 8 (bottom). While the pads for the microwave output signal and the supply, are connected to the top layer lines via gold bond wires, the pads 1, 1', 2, and 2', are connected by two orthogonal, crossed pad-to-pad bond wires, as described in Section II. The YIG sphere is mounted on a beryllium oxide ceramic rod and positioned in the center between the bond wires as well as the pads 1, 1', 2, and 2'.

The setup for measuring the YTO is shown in Fig. 9. The substrate, which contains the YTO, is placed in a laboratory electromagnet with an air gap of about 5 mm. In order to measure the magnetic field, a hall probe of a magnetometer (AlphaLab, Inc. GM1-ST) was placed in the air gap, as well. An additional power supply (HP 6675A) generated the current to produce the dc magnetic field in the air gap. The measurements of the YTO's output signal were performed with a spectrum and phase noise analyzer (R&S FSWP). As the YTO offers a differential output signal, only one output was connected to the single-ended input of the R&S FSWP, while the complementary output was connected to a coaxial 50 Ω load.

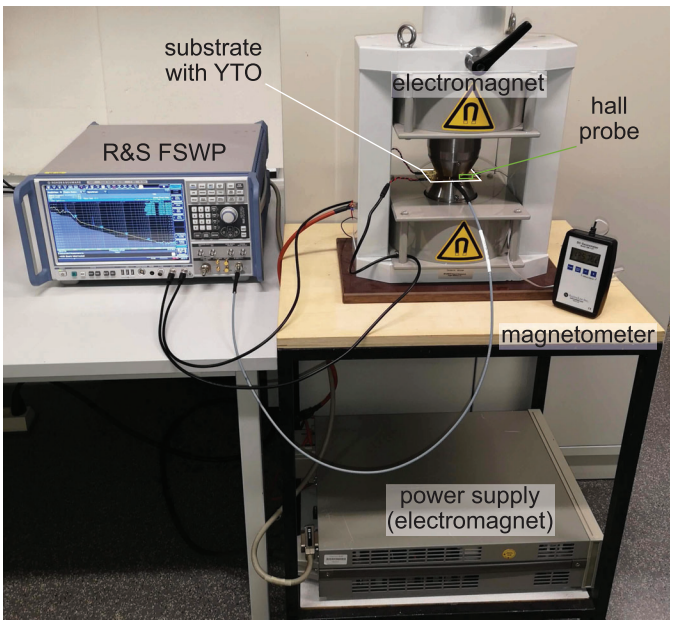

Fig. 9. Photograph of the measurement setup, including phase noise and spectrum analyzer (R&S FSWP), magnetometer with hall sensor and substrate with embedded YIG oscillator placed in the laboratory electromagnet with dedicated power supply.

VI. Results

The results of the YTO with a length of the load transmission line $l_\mathrm{L} = l_\mathrm{L}' = 180$ μm are depicted in Fig. 7 (top) and are comparable to [23]. It reaches a tuning range of 32 GHz $\leq f_\mathrm{osc} \leq$ 48.2 GHz. Yet, these are the highest reported oscillation frequencies of a YTO, which is a result of the short bond wires and the short load transmission line. At the same time, it exhibits an excellent phase noise. For oscillation frequencies $f_\mathrm{osc} \leq 42$ GHz, the phase noise at an offset frequency of $\Delta f = 100$ kHz is only $L_{\Delta f=100\ \mathrm{kHz}} < -119$dBc/Hz and for the entire tuning range it is -130dBc/Hz $\leq L_{\Delta f=100\ \mathrm{kHz}} \leq -92$dBc/Hz.

Although the relative bandwidth for $l_\mathrm{L} = 180$ μm is already 40.4%, the YTO with $l_\mathrm{L} = 260$ μm reaches a relative bandwidth of 73.7% and thus, more than an octave tuning range. As shown in Fig. 10 (bottom), the range of oscillation frequencies is 19.1 GHz $\leq f_\mathrm{osc} \leq$ 41.4 GHz. Again, the YTO exhibits an excellent phase noise. For oscillation frequencies $f_\mathrm{osc} \leq 38$ GHz, the phase noise is only $L_{\Delta f=100\ \mathrm{kHz}} < -120$ dBc/Hz and for the entire tuning range it is -129 dBc/Hz $\leq L_{\Delta f=100\ \mathrm{kHz}} \leq -95$ dBc/Hz. Moreover, the YTO offers a wide range of 19.8 GHz $\leq f_\mathrm{osc} \leq$ 36.5 GHz, where the phase noise is not only very low but also very constant with $L_{\Delta f=100\ \mathrm{kHz}} = (-127 \pm 2)$ dBc/Hz. The constant phase noise within this range gets even more visible in Fig. 11, which shows the phase noise as a function of the offset frequency Δf for various exemplary oscillation frequencies. The traces for the oscillation frequencies within the region of constant phase noise are pretty equal, except for the noise floor at high offset frequencies. This is due to the dissimilar output power at different oscillation frequencies. The flicker noise corner is approximately 30 kHz.

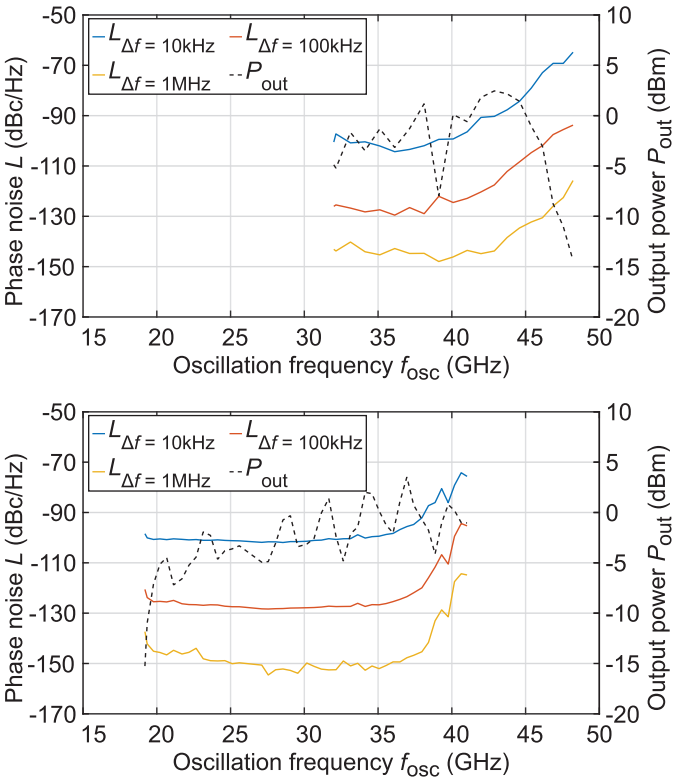

Fig. 10. Measured phase noise L at different offset frequencies Δf and output power P_{out} as a function of the oscillation frequency f_{osc} for the realized YTO with a length of the load transmission line of $l_L = l'_L = 180$ μm (top) and $l_L = l'_L = 260$ μm (bottom).

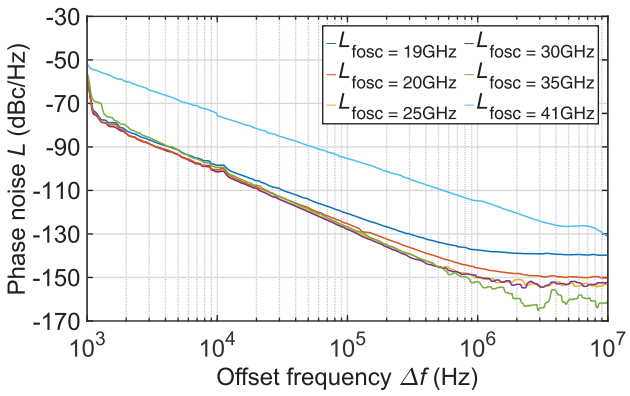

Fig. 11. Measured phase noise L at different oscillation frequencies f_{osc} as a function of the offset frequency Δf for the realized YTO with a length of the load transmission line of $l_L = l'_L = 260$ μm.

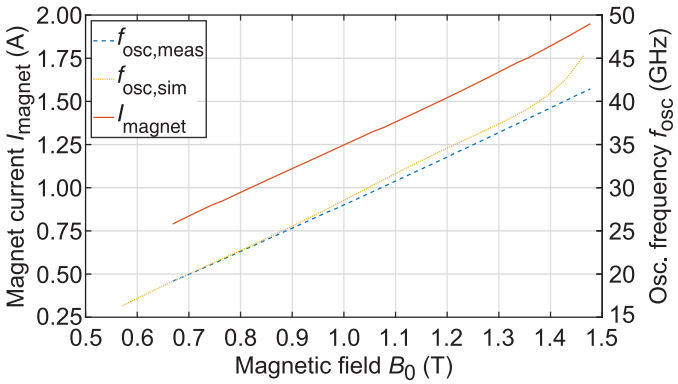

Fig. 12. Measured current injected into the electromagnet I_{magnet} as well as oscillation frequency f_{osc} as a function of the external dc magnetic field $B_0 = \mu \cdot H_0$ for the realized YTO with a length of the load transmission line of $l_L = l'_L = 260$ μm.

Furthermore, Fig. 11 contains the phase noise traces for the oscillation frequencies at the edge of the entire tuning range. While the phase noise at $f_{osc} \approx 19$ GHz is still comparable, the phase noise at $f_{osc} \approx 41$ GHz is increased, but still suitable for low noise applications. The output power of both oscillators is in the same order as it is in the simulations, except from the edge of the tuning range, where the YTO just meets the oscillation condition. However, the output power is varying unexpectedly over the oscillation frequency. This is probably due to an insufficient matching between the MMIC output and the combination of bond wire, transmission line on the substrate, connector, coaxial cable, and external load.

Moreover, Fig. 12 shows the measured and simulated tuning curves, which means the oscillation frequency as a function of the external dc magnetic field $B_0 = \mu \cdot H_0$, as well as the corresponding current injected into the electromagnet I_{magnet} for the YTO with the load transmission line $l_L = l'_L = 260$ μm. As expected from (2), the tuning curve is highly linear. Only at high oscillation frequencies $f_{osc} \gtrsim 40$ GHz, the measured and simulated tuning curves deviate considerably. However, the measured tuning curve is still highly linear, whereas the simulated one gets nonlinear. Including the fact that the realized YTO does not work up to such high oscillation frequencies as the simulated one, we conclude that the YIG resonator model from Section III has a limited accuracy near the self-resonance of the bond wires. However, the tuning range, phase noise, and tuning curve of the realized and simulated YTOs are generally in good agreement. Even the increasing phase noise toward higher oscillation frequencies due to the self-resonance of the bond wires can be observed in the simulations as well as in the measurements. Thus, the YIG resonator model from Section III is appropriate for designing and optimizing of transmission-type YTOs. Moreover, if the electromagnet is turned off, there are no measurable oscillations in the output spectrum. Thus, even in practice with not perfect orthogonal coupling loops, there is no oscillation except from the YIG, as expected in Section IV.

VII. Comparison

Table I gives an overview of the state-of-the-art high-end, wideband tunable oscillators at microwave frequencies. It focuses on YTOs but also includes recent TOEOs and VCOs. While one of the best commercial available YTOs, the MLOS1840 [24], and VCOs, the HMC733 [36], are listed as well, actual no commercial wideband TOEO is offered. The publications of different tunable oscillators in Table I offer different information. The works [24], [27], [28] and [17] only specify the phase noise at single, but not equal, offset frequencies. Whereas, the publications [19], [20] and

TABLE I
COMPARISON OF STATE-OF-THE-ART WIDEBAND TUNABLE OSCILLATORS AT MICROWAVE FREQUENCIES

Ref	Year	Type	Tuning range (GHz)	BW (GHz)	Rel. BW (%)	$L_{\Delta f=10\,\mathrm{kHz}}$ (dBc/Hz)		$L_{\Delta f=100\,\mathrm{kHz}}$ (dBc/Hz)		$L_{\Delta f=1\,\mathrm{MHz}}$ (dBc/Hz)		P_{out} (dBm)	FoM (dB)
						abs.	nor.*	abs.	nor.*	abs.	nor.*		
This work	2019	YTO, SiGe	19.1 ... 41.4	22.3	73.7	−100	−100	−127	−127	−150	−150	−2	248
			32.0 ... 48.2	16.2	40.4	−97	−99	−123	−125	−145	−147	−3	235
[28]	2014	YTO, SiGe	2.0 ... 20.0	18.0	163.6	n/a	n/a	n/a	n/a	−150	−141	0	253
[22]	2017	YTO, discrete	6.0 ... 12.0	6.0	66.7	−110	−100	−133	−123	−155	−145	7	241
[27]	1996	YTO, discrete	3.0 ... 8.5	5.5	95.6	−110	−96	n/a	n/a	n/a	n/a	8	238
[24]	2002	YTO, commercial	18.0 ... 40.0	22.0	75.9	n/a	n/a	−95	−95	n/a	n/a	13	213
[19]	2015	TOEO, f-doubler	8.8 ... 37.6	28.8	124.1	−100	−98	−120	−118	−122	−120	n/a	227
[20]	2013	TOEO, WGMR	2.0 ... 15.0	13.0	152.9	−100	−89	−120	−109	−140	−129	n/a	240
[17]	2018	VCO, SiGe	50.0 ... 72.0	22.0	36.1	n/a	n/a	n/a	n/a	−105	−111	6	197
[18]	2017	VCO, SiGe	6.5 ... 15.1	8.6	79.6	−80	−71	−88	−79	−110	−101	n/a	201
[36]	n/a	VCO, commercial	10.0 ... 20.0	10.0	66.7	−60	−54	−90	−84	−119	−113	3	209

* Phase noise L with center frequency of tuning range normalized to 30 GHz

[18] show the phase noise only at one or two oscillation frequencies, but as a function of the offset frequency. Besides this work, only [22] and [36] specify the phase noise as a function of the oscillation frequency and as a function of the offset frequency. However, to compare the phase noise easily, Table I shows the absolute phase noise as well as a normalized phase noise. The normalized phase noise takes the native increase with the oscillation frequency by 20dB/dec into account. Applying this relationship, for each oscillator, the phase noise at the center frequency of the tuning range was normalized to a center frequency of 30 GHz. Comparing the normalized phase noise with the state-of-the-art oscillators in Table I, this work achieves the best phase noise performance.

Due to the aforementioned unequally, not fully specified phase noise in different works of Table I, the certainly existing deviation of the phase noise over the wide frequency ranges as well as the influence of different flicker noise corners of the tunable oscillators cannot be entirely compared. Moreover, the power consumption is only determined in [18], [24] and [36]. Thus, the comparison by means of the figure-of-merit (FoM) is an indication, which should be considered with caution but does not allow an entire comparison. The FoM is defined as

$$\mathrm{FoM} = \left(\frac{f_{\mathrm{osc}}}{\Delta f}\right)^2 \cdot \left(\frac{\mathrm{Rel.\ BW}}{10}\right)^2 \cdot \frac{1}{L_{\Delta f}}. \tag{9}$$

It is based on the $\mathrm{FoM}_{\mathrm{VCO\text{-}T}}$ defined by the International Technology Roadmap for Semiconductors [37], but has been adapted, due to the not available power consumption. While the FoM of [27] and [24] is calculated at $\Delta f = 10$ kHz and $\Delta f = 100$ kHz, respectively, the FoM of all other tunable oscillators is calculated at $\Delta f = 1$ MHz. This work achieves the second best FoM compared to the state-of-the-art oscillators in Table I. Only [28] exhibits a slightly better FoM. This is just due to the extreme high relative bandwidth of [28], because the normalized phase noise and the absolute bandwidth are not as good as those achieved in this work.

VIII. CONCLUSION

We presented a novel fully differential YIG tuned oscillator, which is based on a SiGe MMIC. The transmission-type YIG resonator is realized by two orthogonal, crossed pad-to-pad bond wires, acting as coupling loops, and a YIG sphere positioned directly between those bond wires and the MMIC. The MMIC contains a common base amplifier as the oscillator core as well as an output buffer. Due to an adjustable transmission line as an inductive load, the range of oscillation frequencies can be slightly shifted. Therefore, we reached a tuning range of 19.1 GHz $\leq f_{\mathrm{osc}} \leq$ 41.4 GHz and 32 GHz $\leq f_{\mathrm{osc}} \leq$ 48.2 GHz for a length of the load transmission line of $l_{\mathrm{L}} = 260\ \mu$m and $l_{\mathrm{L}} = 180\ \mu$m, respectively. Yet, the latter exhibits the highest reported oscillation frequencies of a YTO. Both YTOs exhibit an excellent phase noise. At an offset frequency of $\Delta f = 100$ kHz, the average phase noise is −127dBc/Hz ($l_{\mathrm{L}} = 260\ \mu$m) and −123dBc/Hz ($l_{\mathrm{L}} = 180\ \mu$m) for a frequency range of 19.8 GHz $\leq f_{\mathrm{osc}} \leq$ 36.5 GHz and 30.2 GHz $\leq f_{\mathrm{osc}} \leq$ 42 GHz, respectively. Compared to state-of-the-art high end, wideband tunable oscillators at microwave frequencies, this is the lowest reported phase noise with respect to the dependence of the oscillation frequency. Moreover, we developed an equivalent circuit to model the transmission-type YIG resonator. As the simulations and measurements are in good agreement concerning the tuning range and phase noise of the YTOs, the developed YIG model is appropriate to design and optimize transmission-type YTOs.

ACKNOWLEDGMENT

The authors would like to thank Infineon Technologies AG for fabricating the chips.

REFERENCES

[1] G. Hasenaecker, M. van Delden, T. Jaeschke, N. Pohl, K. Aufinger, and T. Musch, "A SiGe fractional-N frequency synthesizer for mm-wave wideband FMCW radar transceivers," *IEEE Trans. Microw. Theory Techn.*, vol. 64, no. 3, pp. 847–858, Mar. 2016.

[2] K. B. Cooper, R. J. Dengler, N. Llombart, B. Thomas, G. Chattopadhyay, and P. H. Siegel, "THz imaging radar for standoff personnel screening," *IEEE Trans. THz Sci. Technol.*, vol. 1, no. 1, pp. 169–182, Jun. 2011.

[3] K. Statnikov, J. Grzyb, B. Heinemann, and U. R. Pfeiffer, "160-GHz to 1-THz multi-color active imaging with a lens-coupled SiGe HBT chipset," *IEEE Trans. Microw. Theory Techn.*, vol. 63, no. 2, pp. 520–532, Feb. 2015.

[4] F. Herzel, D. Kissinger, and H. J. Ng, "Analysis of ranging precision in an FMCW radar measurement using a phase-locked loop," *IEEE Trans. Circuits Syst., I, Reg. Papers*, vol. 65, no. 2, pp. 783–792, Feb. 2018.

[5] K. Thurn, R. Ebelt, and M. Vossiek, "Noise in homodyne FMCW radar systems and its effects on ranging precision," in *IEEE MTT-S Int. Microw. Symp. Dig.*, Jun. 2013, pp. 1–3.

[6] M. Mallach and T. Musch, "Fast and precise data acquisition for broadband microwave tomography systems," *Meas. Sci. Technol.*, vol. 28, no. 9, pp. 1–14, Sep. 2017.

[7] J. Nehring, M. Dietz, K. Aufinger, G. Fischer, R. Weigel, and D. Kissinger, "A 4–32-GHz chipset for a highly integrated heterodyne two-port vector network analyzer," *IEEE Trans. Microw. Theory Techn.*, vol. 64, no. 3, pp. 892–905, Mar. 2016.

[8] D. A. Hall and A. Hinde, "Understanding the effect of uncorrelated phase noise on the phase coherency of multi-channel RF vector signal analyzers," in *IEEE MTT-S Int. Microw. Symp. Dig.*, Anaheim, CA, USA, May 2010, pp. 592–597.

[9] T. Jaeschke, C. Bredendiek, S. Küppers, and N. Pohl, "High-precision D-band FMCW-radar sensor based on a wideband SiGe-transceiver MMIC," *IEEE Trans. Microw. Theory Techn.*, vol. 62, no. 12, pp. 3582–3597, Dec. 2014.

[10] M. Hitzler *et al.*, "Ultracompact 160-GHz FMCW radar MMIC with fully integrated offset synthesizer," *IEEE Trans. Microw. Theory Techn.*, vol. 65, no. 5, pp. 1682–1691, May 2017.

[11] B. Friederich, T. Schultze, and I. Willms, "A novel approach for material characterization based on a retroreflector wide band transceiver radar," in *Proc. IEEE Int. Conf. Ubiquitous Wireless Broadband (ICUWB)*, Montreal, QC, Canada, Oct. 2015, pp. 1–4.

[12] N. Palka, M. Szala, and E. Czerwinska, "Characterization of prospective explosive materials using terahertz time-domain spectroscopy," *Appl. Opt.*, vol. 55, no. 17, pp. 4575–4583, Jun. 2016.

[13] S. Pisa, E. Pittella, and E. Piuzzi, "A survey of radar systems for medical applications," *IEEE Aerosp. Electron. Syst. Mag.*, vol. 31, no. 11, pp. 64–81, Nov. 2016.

[14] Q. Cassar *et al.*, "Pilot study of freshly excised breast tissue response in the 300–600 GHz range," *Biomed. Opt. Express*, vol. 9, no. 7, pp. 2930–2942, Jul. 2018.

[15] M. Mallach, M. Oberberg, P. Awakowicz, and T. Musch, "Fast broadband reflectometer for diagnostics of plasma processes based on spatially distributed multipole resonance probes," in *Proc. IEEE MTT-S Int. Microw. Symp. (IMS)*, Honolulu, HI, USA, Jun. 2017, pp. 1022–1025.

[16] R. Best, *Phase-Locked Loops*, 6th ed. New York, NY, USA: McGraw-Hill, 2007.

[17] M. van Delden, N. Pohl, and T. Musch, "An ultra-wideband fast frequency ramp synthesizer at 60 GHz with low noise using a new loop gain compensation technique," *IEEE Trans. Microw. Theory Techn.*, vol. 66, no. 9, pp. 3937–3946, Sep. 2018.

[18] T. Drechsel, N. Joram, and F. Ellinger, "A 6.5 to 15.1 GHz ultra-wideband SiGe LC VCO with 80 % continuous tuning range," in *Proc. Eur. Conf. Circuit Theory Design (ECCTD)*, Catania, Italy, Sep. 2017, pp. 1–4.

[19] W. Li, J. G. Liu, and N. H. Zhu, "A widely and continuously tunable frequency doubling optoelectronic oscillator," *IEEE Photon. Technol. Lett.*, vol. 27, no. 13, pp. 1461–1464, Jul. 1, 2015.

[20] D. Eliyahu *et al.*, "Resonant widely tunable opto-electronic oscillator," *IEEE Photon. Technol. Lett.*, vol. 25, no. 15, pp. 1535–1538, Aug. 1, 2013.

[21] P. S. Carter, "Equivalent circuit of orthogonal-loop-coupled magnetic resonance filters and bandwidth narrowing due to coupling inductance," *IEEE Trans. Microw. Theory Techn.*, vol. 18, no. 2, pp. 100–105, Feb. 1970.

[22] W. Stein, F. Huber, S. Bildik, M. Aigle, and M. Vossiek, "An improved ultra-low-phase noise tunable YIG oscillator operating in the 6–12 GHz range," in *Proc. 47th Eur. Microw. Conf. (EuMC)*, Nuremberg, Germany, Oct. 2017, pp. 767–770.

[23] M. van Delden, N. Pohl, K. Aufinger, and T. Musch, "A 32-48 GHz differential YIG oscillator with low phase noise based on a SiGe MMIC," in *Proc. IEEE Radio Wireless Symp. (RWS)*, Orlando, FL, USA, Jan. 2019, pp. 1–3.

[24] Micro Lambda Wireless, Inc. (Mar. 2019). *MLOS Series 40 GHz YIG Tuned Oscillators Millimeter Wave*. [Online]. Available: https://www.microlambdawireless.com/uploads/pdfs/MLOS1840,2040,2640-Copy1.pdf

[25] M. Rytel, P. Kopyt, and B. Salski, "Phase locked loop Ku band frequency synthesizer based on a tuned YIG oscillator," in *Proc. 22nd Int. Microw. Radar Conf. (MIKON)*, Poznan, Poland, May 2018, pp. 434–437.

[26] M. Fanesi, R. Tosini, M. Gris, B. Gabbrielli, and T. Rozzi, "A compact, low cost, low power YIG synthesiser for long haul applications," in *Proc. 31st Eur. Microw. Conf.*, London, U.K., Sep. 2001, pp. 1–4.

[27] T. Musch, "A low noise and low cost YIG-oscillator in the frequency range from 4.5 GHz to 12 GHz," in *Proc. 26th Eur. Microw. Conf.*, Prague, Czech Republic, Sep. 1996, pp. 81–85.

[28] A. A. Sweet and R. Parrott, "A wide band, low phase noise, differential YIG tuned oscillator," in *Proc. WAMICON*, Tampa, FL, USA, Jun. 2014, pp. 1–3.

[29] P. Röschmann, "YIG filter," *Philips Tech. Rev.*, vol. 32, no. 9, pp. 322–327, 1971.

[30] P. S. Carter, "Magnetically-tunable microwave filters using single-crystal yttrium-iron-garnet resonators," *IRE Trans. Microw. Theory Techn.*, vol. 9, no. 3, pp. 252–260, May 1961.

[31] L. R. Walker, "Resonant modes of ferromagnetic spheroids," *J. Appl. Phys.*, vol. 29, no. 3, pp. 318–323, Mar. 1958.

[32] H. Maier-Flaig *et al.*, "Temperature-dependent magnetic damping of yttrium iron garnet spheres," *Phys. Rev. B, Condens. Matter*, vol. 95, no. 21, Jun. 2017, Art. no. 214423.

[33] E. G. Spencer, R. C. LeCraw, and A. M. Clogston, "Low-temperature line-width maximum in yttrium iron garnet," *Phys. Rev. Lett.*, vol. 3, no. 1, pp. 32–33, Jul. 1959.

[34] J. Böck *et al.*, "SiGe HBT and BiCMOS process integration optimization within the DOTSEVEN project," in *Proc. IEEE Bipolar/BiCMOS Circuits Technol. Meeting (BCTM)*, Boston, MA, USA, Oct. 2015, pp. 121–124.

[35] U. Tietze and C. Schenk, *Electronic Circuit*, 2nd ed. Heidelberg, Germany: Springer, 2008.

[36] Analog Devices, Inc. (Mar. 2019). *HMC733LC4B wideband MMIC VCO w/bufferamplifier,10–20 GHz*. [Online]. Available: https://www.analog.com/media/en/technical-documentation/data-sheets/hmc733.pdf

[37] *ITRS 2011 Edition System Drivers*, Int. Roadmap Devices Syst., Piscataway, NJ, USA, 2011.

Marcel van Delden (S'14) was born in Hattingen, Germany, in 1990. He received the B.Sc. and M.Sc. degrees in electrical engineering from Ruhr University Bochum, Bochum, Germany, in 2012 and 2015, respectively.

Since October 2013, he has been a Research Assistant with the Institute of Electronic Circuits, Ruhr University Bochum. His current research interests include the design of integrated mm-wave and digital circuits in ultra-wideband frequency synthesis with highest phase stability.

Nils Pohl (GS'07–M'11–SM'14) received the Dipl.-Ing. and Dr.-Ing. degrees in electrical engineering from Ruhr University Bochum, Bochum, Germany, in 2005 and 2010, respectively.

From 2006 to 2011, he was a Research Assistant with Ruhr University Bochum, where he was involved in integrated circuits for millimeter-wave radar applications. In 2011, he became an Assistant Professor with Ruhr University Bochum, and in 2013, he became the Head of the Department of Millimeter Wave Radar and High Frequency Sensors, Fraunhofer Institute for High Frequency Physics and Radar Techniques, Wachtberg, Germany. In 2016, he became a Full Professor of integrated systems with Ruhr University Bochum. He has authored or coauthored more than 100 scientific papers and has issued several patents. His current research interests include ultra-wideband millimeter-wave radar, design and optimization of millimeter-wave integrated SiGe circuits and system concepts with frequencies up to 240 GHz and above, as well as frequency synthesis and antennas.

Dr. Pohl is a member of VDE, ITG, EUMA, and URSI. He was a recipient of the Karl-Arnold Award of the North Rhine-Westphalian Academy of Sciences, Humanities, and the Arts in 2013. He was a co-recipient of the 2009 EEEfCom Innovation Award, the 2012 EuMIC Prize, and the 2015 Best Demo Award of IEEE Radio Wireless Week.

Klaus Aufinger (M'09) received the Diploma and Ph.D. degrees in physics from the University of Innsbruck, Innsbruck, Austria, in 1990 and 2001, respectively.

From 1990 to 1991, he was a Teaching Assistant with the Institute of Theoretical Physics, University of Innsbruck. In 1991, he joined Corporate Research and Development, Siemens AG, Munich, Germany, where he was involved in the investigation of noise in submicrometer bipolar transistors. He is currently with Infineon Technologies AG, Neubiberg, Germany, where he is involved with device physics, technology development, and the modeling of advanced SiGe technologies for high-speed digital and analog circuits.

Christoph Baer (S'13–M'16) received the Dipl.-Ing. and Dr.-Ing. degrees in electrical engineering from Ruhr University Bochum, Bochum, Germany, in 2009 and 2015, respectively.

From 2006 to 2015, he was an RF Research Engineer with the Krohne Group, Duisburg, Germany. In 2015, he became a Post-Doctoral Researcher with Ruhr University Bochum. Since 2016, he has been an Academic Counselor with the Institute of Electronic Circuits, Ruhr University Bochum. He has authored or coauthored more than 60 scientific papers and holds several patents. His current research interests include radar systems, humanitarian demining sensors, antenna design, and material characterization and synthesis.

Dr. Baer is the founder and current Chair of the IEEE SIGHT Germany Section.

Thomas Musch (M'06) was born in Mülheim Ruhr, Germany, in 1968. He received the Dipl.-Ing. and Dr.Ing. degrees in electrical engineering from Ruhr University Bochum, Bochum, Germany, in 1994 and 1999, respectively.

From 1994 to 2000, he was a Research Assistant with the Institute of High Frequency Engineering, Ruhr University Bochum, where he was involved in system concepts and electronic components at microwave frequencies, especially frequency synthesis and high-precision radar. From 2003 to 2008, he was with Krohne Messtechnik GmbH, Duisburg, Germany. As the Head of the Department of Corporate Research, he was responsible for research activities with the Krohne Group, Duisburg. In 2008, he became a Full Professor of electronic circuits with Ruhr University Bochum. His current research interests include frequency synthesis, radar systems and antennas for microwave range findings, industrial applications of microwaves, and automotive electronics.